

Volume Transport Estimation of the Kuroshio Extension based on Subsurface Mooring Array and Satellite Altimetry

Haihong Guo¹, Zhaohui Chen², Haiyuan Yang², Yu Long³, Ruichen Zhu², Yue-Qi Zhang¹, and Zhao Jing¹

¹Ocean University of China

²Physical Oceanography Laboratory, Ocean University of China

³State Key Laboratory of Satellite Ocean Environment Dynamics, Second Institute of Oceanography

December 20, 2022

Abstract

The vertical structure of the Kuroshio Extension (KE) is investigated using velocity measurements from a subsurface mooring array. Mode decomposition based on climatological Temperature/Salinity (T/S) data shows that the barotropic and first baroclinic normal modes dominate the vertical structure of the zonal flow in the KE. This structure is also well described by the leading mode of Empirical Orthogonal Functions (EOFs) that contains the first two vertical normal modes. Further analysis demonstrates that the projection coefficient of the mooring velocity onto the summed vertical mode could be well represented by the surface geostrophic velocity. Therefore, we propose a dynamic method that relates the surface geostrophic flow and the vertical structure of the zonal flow. The applicability of this method is verified with both reanalysis datasets and estimation from hydrographic data. The findings implicate that the KE transport can be well reproduced by surface geostrophic flow and climatological T/S data only.

Hosted file

952418_0_art_file_10546332_rn4pwd.docx available at <https://authorea.com/users/567895/articles/613997-volume-transport-estimation-of-the-kuroshio-extension-based-on-subsurface-mooring-array-and-satellite-altimetry>

Hosted file

952418_0_supp_10546334_rn4pnk.docx available at <https://authorea.com/users/567895/articles/613997-volume-transport-estimation-of-the-kuroshio-extension-based-on-subsurface-mooring-array-and-satellite-altimetry>

1
2 **Volume Transport Estimation of the Kuroshio Extension based on Subsurface**
3 **Mooring Array and Satellite Altimetry**

4 **Haihong Guo^{1,2}, Zhaohui Chen^{1,2*}, Haiyuan Yang^{1,2}, Yu Long³, Ruichen Zhu^{1,2}, Yueqi**
5 **Zhang^{1,2}, Zhao Jing^{1,2}**

6 ¹Laoshan Laboratory, Qingdao, China.

7 ²Frontier Science Center for Deep Ocean Multi-spheres and Earth System (FDOMES)
8 and Physical Oceanography Laboratory, Ocean University of China, Qingdao, China.

9 ³State Key Laboratory of Satellite Ocean Environment Dynamics, Second Institute of
10 Oceanography, Ministry of Natural Resources, Hangzhou 310012, China.

11 Corresponding author: Zhaohui Chen (chenzhaohui@ouc.edu.cn)

12 **Key Points:**

- 13 • The vertical structure of the Kuroshio Extension is dominated by the barotropic and first
14 baroclinic normal modes.
- 15 • The leading mode of Empirical Orthogonal Functions contains the first two vertical
16 normal modes.
- 17 • The Kuroshio Extension transport can be well reproduced by surface geostrophic flow
18 and hydrographic data.
19

20 **Abstract**

21 The vertical structure of the Kuroshio Extension (KE) is investigated using velocity
22 measurements from a subsurface mooring array. Mode decomposition based on climatological
23 Temperature/Salinity (T/S) data shows that the barotropic and first baroclinic normal modes
24 dominate the vertical structure of the zonal flow in the KE. This structure is also well described
25 by the leading mode of Empirical Orthogonal Functions (EOFs) that contains the first two
26 vertical normal modes. Further analysis demonstrates that the projection coefficient of the
27 mooring velocity onto the summed vertical mode could be well represented by the surface
28 geostrophic velocity. Therefore, we propose a dynamic method that relates the surface
29 geostrophic flow and the vertical structure of the zonal flow. The applicability of this method is
30 verified with both reanalysis datasets and estimation from hydrographic data. The findings
31 implicate that the KE transport can be well reproduced by surface geostrophic flow and
32 climatological T/S data only.

33 **Plain Language Summary**

34 The Kuroshio Extension (KE) plays an important role in the mid-latitude North Pacific climate
35 system. To better understand the KE dynamic and its influences, it is very important to estimate
36 the KE transport. However, direct observation is very difficult in this area. Combining a
37 subsurface mooring array and satellite altimetry, the vertical scale of the KE is explored in this
38 study using mode decomposition methods. The vertical structure of the KE is dominated by the
39 barotropic and first baroclinic modes. The relationship between the vertical structure of the zonal
40 velocity and surface geostrophic flow in the KE region is further investigated. Based on this
41 relationship, the KE transport can be well estimated by surface geostrophic flow and
42 hydrographic data.

43 **1 Introduction**

44
45 The Kuroshio Current (KC), which originates from the Philippines coast and leaves the
46 Japanese archipelago in the midlatitude ocean, acts as a mass, momentum, and heat conveyor
47 connecting the tropical and extratropical Northern Pacific Ocean. After leaving the western
48 boundary, the Kuroshio veers eastward as a zonal flow, i.e., the Kuroshio Extension (KE) jet.
49 This eastward jet builds a sharp potential vorticity front and a temperature front in the mid-
50 latitude North Pacific, resulting in abundant shedding of eddies through baroclinic/barotropic
51 instability (Hurlburt et al., 1996). These eddies draw (return) energy from (to) the mean flow in
52 the upstream (downstream) KE (Yang et al., 2017). In addition to rich oceanic processes, the KE
53 has also been regarded as an important region of coupled ocean-atmosphere activities (O'Reilly
54 and Czaja, 2014). Qiu (2003) showed that the KE is remotely forced by wind stress curl
55 anomalies related to the Pacific Decadal Oscillation (PDO). Besides, the feedback between ocean
56 mesoscale eddies and the atmosphere is fundamental to the dynamics of the KE jet (Ma et al.,
57 2015).

58 The KE plays an important role in modulating the environmental features from the surface
59 to the deep layer (Bishop et al., 2012; Yang et al., 2021). In the surface layer, as a typical
60 subtropical western boundary extension, the KE is a hot spot of high marine heat wave intensity
61 with large sea surface temperature variability (Oliver et al., 2021). In the lower layer, the KE is a
62 critical source of the North Pacific intermediate water (NPIW), characterized by a vertical
63 salinity minimum (Hiroe et al., 2002), which is important for the carbon cycle between subarctic

64 and subtropic (Tsunogai et al., 2002). Besides, the deep convection that occurs in the KE region
65 forms vertically homogeneous water, the Subtropical Mode Water (STMW). The STMW is
66 carried away from its formation area and widely distributed (Suga and Hanawa, 1995). In the
67 deep layer, evidence was found that the abyssal currents are weakly bottom intensified (Bishop
68 et al., 2012). Therefore, in the KE region, abundant multi-scale oceanic processes and air-sea
69 interactions play an essential role in the extratropical North Pacific climate system (Jayne et al.,
70 2009; Kida et al., 2015; Ma et al., 2015; Qiu et al., 2007;). However, the vertical scale of the KE
71 remains poorly understood and requires more observational evidence.

72 Moreover, to better understand the role of the Kuroshio in the climate system, it is
73 necessary to first reveal the mass/heat transport meridionally and zonally. Along the Kuroshio
74 pathway, there have long been numerous hydrographic and current observations in the past
75 decades near the Philippines coast, east of Taiwan island, the Eastern China Sea (ECS) shelf
76 break, south of Japan. However, in the KE region, directly observed transport for the Kuroshio in
77 this region has been lacking due to the complex structure, strong currents, and rich eddies, which
78 pose a serious challenge for in-situ observation. Despite these difficulties, there have been
79 several types of observations that have captured the KE transport. Using the hydrographic data
80 occupied across the Kuroshio extension along the longitudes of 165°E, Joyce (1987) provided an
81 estimation of the eastward KE transport (56 ± 2 Sv). Based on a current meter mooring, Hall
82 (1989) more directly measured the transport of the KE with a value of 87 ± 21 Sv. Furthermore,
83 Yoshikawa et al. (2004) calculated transport of 163 Sv across 146°25'E and 113 Sv across
84 152°30'E using Lowered ADCP data. More systematical observations from the Kuroshio
85 Extension System Study (KESS) project were used to estimate a total downstream transport of
86 114 ± 13 Sv and a weaker Eulerian averaging transport of 79 Sv for the KE (Jayne et al., 2009).
87 Except for direct observation, the surface transport of the KE is linearly related to the SSH
88 difference across the KE (Qiu 2003), which provided a reasonable proxy of the KE strength.
89 However, it is easy to note that these estimations are quite different in time and space. Given the
90 insufficient observations in this area, the biases between different observations are hard to
91 reduce, not to mention the long-term volume transport. To better understand the role of the KE in
92 modulating the ocean and atmosphere, it is necessary to quantify the volume transport of the KE
93 as well as the vertical structure.

94 There have been several projects and sections that provided a valuable estimation of the KE
95 transport. For example, the KESS project employed inverted echo sounders with bottom pressure
96 gauges and current meters (C-PIES), subsurface moorings, Kuroshio Extension Observatory
97 (KEO) surface buoy, and dozens of Argo profiling floats, which could provide a good estimation
98 for the KE. In the SubArctic Gyre Experiment (SAGE), intensive observations were conducted
99 in the KE region with ADCPs/CTDs (Yasuda 2004), which provide an estimation of the volume
100 transport in the intermediate layer (Talley et al., 1995; Hiroe et al., 2002). However, the long-
101 term variabilities of the total KE transport remain unclear. Therefore, longer observations are
102 needed to provide a comprehensive view of the complex circulation in the KE region. Since
103 2015, China has initiated the Kuroshio Extension Mooring System (KEMS, <https://cn-kems.net/>)
104 with an array of subsurface moorings across the KE. (Figure 1, detailed information is provided
105 in the following section). The advantage of a subsurface mooring array is that it can provide a
106 direct long-term observation and cover the full velocity of the upper and some deep flow
107 information.

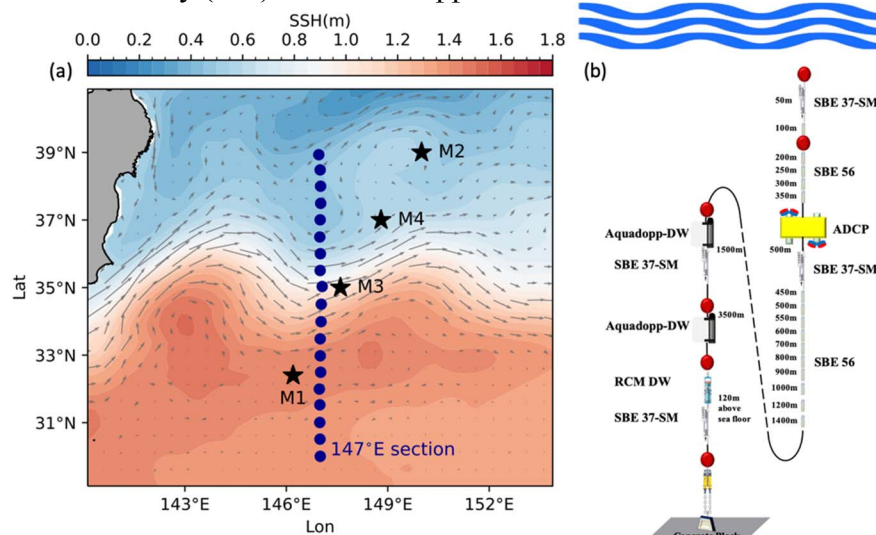
108 It is noteworthy that limited subsurface moorings are sparsely deployed in the KEMS
109 array with over 200 km between each mooring, which makes it hard to directly calculate the KE

110 transport. The main purpose of this paper is to explore the dynamic relationship between the
 111 vertical structure of the observed velocity and the surface geostrophic flow by combing the
 112 climatology hydrographic and altimetry data. Then, an estimation method of volume transport is
 113 extended to calculate the KE transport based on this dynamic relationship. The paper is
 114 organized as follows: Data and methods are first described in Section 2, followed by presenting
 115 the results of the vertical structure, its connections with the geostrophic flow, and the volume
 116 transport estimation in section 3. Finally, in section 4, we will summarize the results.

117 2 Data and method

118 2.1 KEMS Mooring Data

119 As part of the KEMS project, five subsurface moorings were successively deployed along a
 120 line crossing the axis of the KE since 2015. Following the last cruise in July 2022, there are now
 121 five subsurface moorings (M1, M2, M3, M4, and M5), which range from 32.4°N, 146.2°E to
 122 41.0°N, 151.2°E. The KE jet crosses over the mooring array (Figure 1a) with the M3 mooring
 123 being located at the axis. It should be noted that M5 is far away from the axis of the KE jet,
 124 which is not used in this study. In 2015, M1 was deployed at a water depth of ~5600 m with two
 125 ADCPs (RDI Workhorse Long Ranger 75 kHz), four CTDs (SBE 37-SM), three Aquadopp-
 126 DW/SeaguardRCM current meters, and a chain of SeaBird56 temperature loggers equipped
 127 (Figure 1b). Until the last recovery, the longest-running mooring, M1, had been maintained for
 128 almost 7 years, and even the shortest-running mooring used in this study (M4) had been
 129 maintained for more than 2 years. Therefore, these moorings could provide in situ current and
 130 temperature/practical salinity (T/S) data in the upper 1500 m ocean.



131
 132 Figure 1 (a) Locations of KEMS subsurface moorings (black stars) from November 2015 to July
 133 2022. The blue dots denote a historical hydrographic section (147°E) used for comparison in this
 134 study. The color shading and gray arrows represent the climatological sea surface height (SSH)
 135 and the surface geostrophic current. (b) Schematic of the design of the moorings.

136 The velocity data used in this study is mainly obtained by the ADCPs, which were deployed
 137 at around 500-m depth, with one looking upward and the other downward, which could roughly
 138 cover the upper 1000 m. Their sampling interval and vertical bin size were set to 1 hour and 16
 139 m, respectively. The ADCPs records were interpolated vertically onto a standard depth of 10 m

140 intervals. Moreover, three current meters (CM) were deployed at 1500, 3500, and 5500 m after
 141 2016. The sampling intervals of the temperature chain, CTDs, and current meters are 1, 5, and 30
 142 min, respectively. All instrumental data were filtered with a cutoff period of 2 days (the local
 143 inertial period is ~ 22 h) to remove the tidal effect and other high-frequency motions such as
 144 inertial gravity waves.

145 2.2 Other Datasets

146 Since the moorings are located relatively far away from each other, the KE could not be
 147 well covered. More datasets are needed to establish and examine the dynamic mechanism.
 148 Therefore, the gridded daily altimeter data with a spatial resolution of $1/4^\circ$ from Archiving,
 149 Validation, and Interpretation of Satellite Data in Oceanography (AVISO)
 150 (<https://www.aviso.altimetry.fr/>) is used to provide the absolute surface geostrophic current
 151 (Ducet et al., 2000). The AVISO dataset started in 1993 and has been updated to the present. To
 152 explore the vertical structure of the KE, the monthly climatological World Ocean Atlas
 153 (WOA18) temperature and salinity (Locarnini et al., 2018; Zweng et al., 2019) were used to
 154 perform vertical mode decomposition analysis. The stratification used for the decomposition is
 155 calculated by using the WOA 18 T/S data within a 0.5° -radius circle centered at the mooring site
 156 where the monthly climatological data is interpolated into the daily field. It should be noted that
 157 the WOA18 only provides monthly climatological T/S profiles in the upper 1500 m. Therefore,
 158 the profiles below 1500 m are replaced by climatological means. We also use the eddy-resolving
 159 simulations of the Oceanic General Circulation Model for the Earth Simulator (OFES) to further
 160 validate the dynamic mechanism between surface geostrophic flow and vertical structure of the
 161 horizontal velocities (Masumoto et al., 2004). The OFES was spun up for 50 years and integrated
 162 forward from 1950 using daily surface forcing of the National Centers for Environmental
 163 Prediction/National Center for Atmospheric Research (NCEP/NCAR) reanalysis product
 164 (Kalnay et al., 1996). In this study, we only used the OFES data after 1993 to match the same
 165 period with the AVISO data for comparison. The absolute geostrophic velocities derived from
 166 the WOA18 represent the monthly climatological background flow. To test the applicability of
 167 this method, absolute geostrophic velocity data based on hydrographic data at the 147°E line is
 168 used for comparison (Long et al., 2018; Long et al., 2019).

169 2.3 Vertical Normal Mode Decomposition

170 To investigate the vertical structure of the KE, we first employed vertical normal mode
 171 decomposition for the horizontal velocity. In the linearized hydrostatic equations, the vertical
 172 components of the horizontal velocity (u , v) and the pressure field (p) in terms of an
 173 eigenfunction can be projected onto complete orthogonal bases (Vallis, 2017) that satisfies:

$$174 \quad \frac{d}{dz} \left(\frac{1}{N^2} \frac{dC_n(z)}{dz} \right) + \frac{1}{c_n^2} C_n(z) = 0, \quad (1a)$$

$$175 \quad \frac{d}{dz} C_n(0) = -\frac{d}{dz} C_n(-H) = 0, \quad (1b)$$

176 where C_n are the orthogonal bases, c_n are the eigen speeds, and N is the buoyancy frequency
 177 associated with the mean background stratification. The projected intensity of each normalized
 178 baroclinic mode on the horizontal velocity $v(z, t)$ is determined by

$$179 \quad P_{nv}(t) = \frac{\int_H^0 v(z, t) C_n(z) dz}{\int_H^0 C_n^2(z) dz}, \quad (2a)$$

$$v_n(z, t) = C_n(z)P_n(t), \quad (2b)$$

180 where $P_n(t)$ is the projection coefficient of the zonal velocity, representing how strongly the
 181 observed velocity projected onto each mode, and $v_n(z, t)$ is the velocity anomaly of the n th
 182 baroclinic mode (Ma et al., 2022). The explained contribution of each mode can be calculated
 183 by the variance ratio between the mode velocity and full velocity.
 184

185 2.4 The EOF Decomposition

186 Empirical Orthogonal Functions (EOFs) were also used to extract the dominant vertical
 187 structure of the observed full-depth zonal velocity. The climatologic mean of the moored
 188 velocity at each depth was removed before EOF decomposition. It should be noted that the EOF
 189 decomposition does not require additional hydrostatic information (T/S) like the vertical mode
 190 decomposition. Therefore, it could not provide a distinct decomposition with different normal
 191 modes like the vertical normal mode. However, the main EOF mode usually contains a mixing of
 192 different vertical normal modes (Ren et al., 2018). The benefit of EOF decomposition is that it
 193 could explain larger variance in a single mode, which makes it easier to connect the principal
 194 component (PC) series with the surface geostrophic flow. However, EOF decomposition is a
 195 purely statistical method that first requires the local velocity and is hence impossible to achieve
 196 the decomposition except for the mooring position. Therefore, it is instructive to combine these
 197 two methods and take their individual advantages.

198

199 3 Results

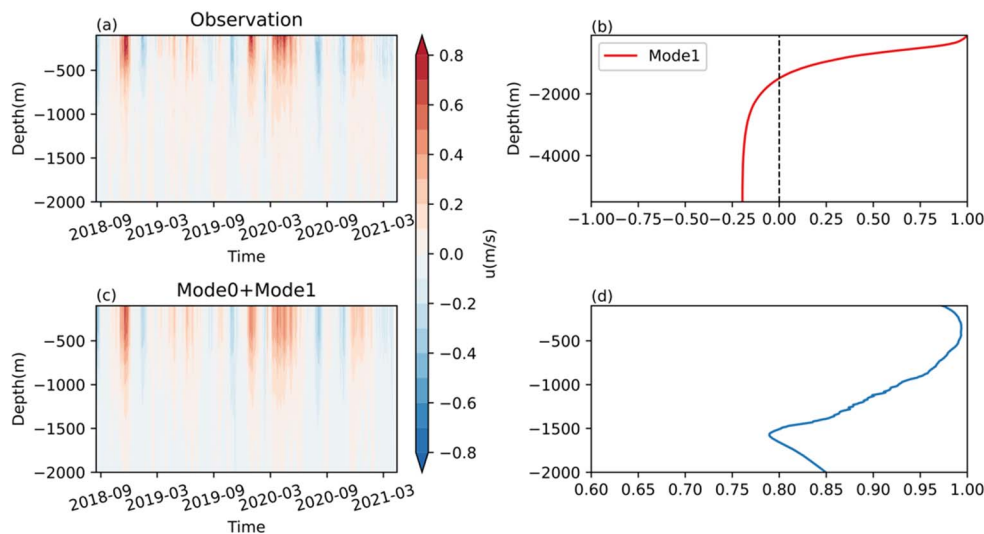
200 In this section, we first employ the vertical mode and EOF decompositions for the zonal
 201 velocity of M1 in sections 3.1 and 3.2. To explore the relationship between these two methods, a
 202 mixed vertical normal mode was deduced to connect these two vertical modes in section 3.3.
 203 Then we extended it to other mooring sites in section 3.4. The dynamic relationship is further
 204 verified by using the OFES dataset in section 3.5. Section 3.6 presents the KE transport
 205 estimation based on vertical modes.

206 3.1 Vertical Normal Modes

207 The southernmost site, M1, was discussed in this part. Before exploring the vertical modes
 208 and their variability, it is necessary to provide an overview of the full velocities. Figure 2a shows
 209 the depth-time plots of the observed daily mean zonal velocity at the M1 site. The zonal flow at
 210 this site is mainly located in the upper 1500 m, where a maximum daily mean velocity of up to
 211 0.98 m/s is observed near the surface. To better elucidate the vertical structure, we apply the
 212 vertical normal mode decomposition at this site (Equation 1) based on WOA18. The mooring
 213 temperature chain was also used in the decomposition, whose vertical mode is very similar to the
 214 WOA18 data. Besides, in order to extend this method into other regions, it is better to keep using
 215 WOA18 data and validate its adaptability. Then, we project the zonal velocity onto vertical
 216 modes to compare it with the surface geostrophic flow by using Equation 2.

217 The mode decomposition shows that the vertical structure of the horizontal velocity is
 218 dominated by the barotropic mode and the first baroclinic mode. The barotropic mode was
 219 normalized to 1 (not shown), which could explain 25% of the total variance. The first baroclinic
 220 mode is significantly surface-intensified with a zero crossing at 1500 m, which explains 57%
 221 variance for the zonal velocity above the zero crossing (Figure 2b). Therefore, the first two

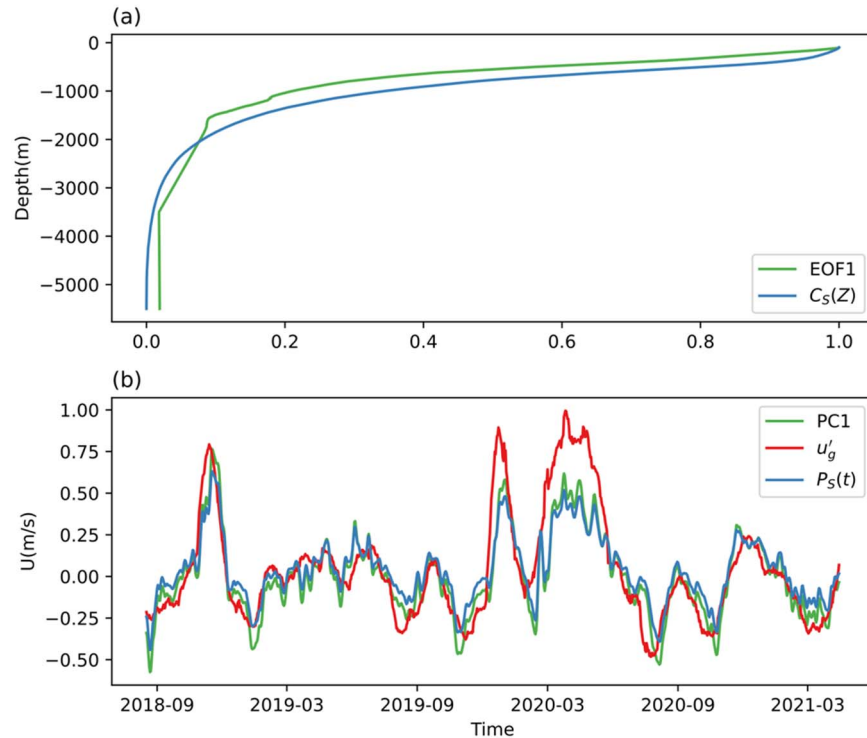
222 modes could explain over 80% variance (Table 1), and dominate the main variability of the zonal
 223 velocity at M1. We sum up these two modes to reproduce the zonal velocities. The summation
 224 could well reproduce the zonal velocity, including the strength, variability, and vertical structure
 225 (Figure 2a, c). It is noteworthy that the reproduced velocity is not exactly consistent with the
 226 geostrophic flow during some periods (February 2020 and May 2020). A more detailed check
 227 shows that these differences are due to nonlocal eddies originating away from the mooring
 228 (Supplementary Figure 1). These eddies could trap fluid parcels and come from other regions
 229 (Zhang et al., 2014), which will bring remote T/S signals and break the local mode
 230 decomposition. Nevertheless, the reproduced velocity correlates well with the moored velocity
 231 with correlations ranging from 0.79 to 0.99 at different depths. The correlation slightly decreases
 232 as depth increases, where a minimum occurs at around the depth of zero-crossing, but it still
 233 reaches 0.79. We can confidently suggest that these two modes dominate the variability of
 234 velocity at M1.



235 Figure 2 (a) The observed zonal velocity at the M1 site. (b) The vertical structure of the first
 236 baroclinic mode. (c) Reconstructed zonal velocity based on the sum of zonal velocity projected
 237 onto barotropic and first baroclinic modes. (d) The correlation between observed velocity and
 238 reconstructed velocity at each depth.
 239
 240

241 3.2 EOF Modes

242 To better understand the vertical structure of the horizontal velocity and how the different
 243 vertical modes mix, we use EOF analysis to further decompose the complex variability patterns.
 244 It is found that the dominant EOF mode tends to mix different vertical normal modes (Ren et al.,
 245 2018), where a direct connection between the AVISO geostrophic velocity and mooring velocity
 246 should be easier to establish. Figure 3 shows the mode-1 EOF (EOF1) of the zonal velocity at
 247 M1 and its principal component (PC1). The EOF1 could explain 92% of the total variance of
 248 mooring velocity, which is similar to the variance contribution of the first two vertical normal
 249 modes (Table 1). The correlation between the PC1 of zonal velocity and AVISO geostrophic
 250 velocity reaches 0.87.



251
 252 Figure 3 (a) The vertical structure of the EOF1 (green) and summed barotropic and first baroclinic
 253 normal mode (blue) at the M1 site. (b) The projection coefficients of the moored zonal velocity
 254 onto EOF1 (green) and the summed vertical normal mode (blue), and the time series of the surface
 255 zonal geostrophic velocity at the M1 site (red).

256 The explained variance shows that the EOF1 contains a mix of barotropic and first
 257 baroclinic modes in the KE region. This is not surprising, since EOF analysis is a
 258 purely statistical method without further dynamic information. The vertical normal mode could
 259 provide detailed information by considering the hydrostatic data and obtaining diverse modes.
 260 Therefore, unlike the EOF mode with orthogonality, the vertical normal mode is also constrained
 261 by the vertical boundary condition, which results in diverse modes. For example, the EOF1 mode
 262 captures in-phase variability of the zonal velocity, while the barotropic mode requires not only
 263 in-phase but also uniform distribution in depth. However, each vertical normal mode corresponds
 264 to an independent time series ($P_n(t)$ in Equation 2a), which is hard to compare with the AVISO
 265 geostrophic flow. The EOF decomposition could reproduce the main feature of zonal velocity by
 266 using a single mode but highly depends on the in-situ observation, which makes it impossible to
 267 predict the structure of the KE other than the mooring site. Therefore, we will explore the
 268 connection between these two mode decomposition methods in the next section.

269 3.3 Mixed Vertical Modes

270 Before investigating the connection between the two mode decomposition methods, it is
 271 useful to consider their similarities and differences. Both the first baroclinic mode and the EOF
 272 mode are surface intensified (Figure 2b, 3a). However, the sign of the velocity of the first
 273 baroclinic mode reverses in the deep ocean, while the EOF1 mode just decays as depth increases.
 274 Given that the strength of the full velocity in the deep layer is much weaker than the upper layer,
 275 and the higher baroclinic modes make a little contribution, the reversed flow of the first
 276 baroclinic mode could be treated as a balance of the barotropic mode in the deep ocean. The

277 mode decomposition also shows that the first baroclinic mode is in the same direction as the
 278 barotropic mode (uniformly identical to 1, not shown) in the upper layer and reverses in the deep
 279 layer (Figure 2b). Therefore, the barotropic component tends to strengthen the upper layer flow
 280 and cancel the deep layer flow of the first baroclinic component. It is well known that the first
 281 baroclinic mode dominates the vertical structure in the world ocean (Chelton et al., 1998).
 282 However, in the KE region, using this single mode will underestimate the full velocity, since the
 283 barotropic mode could explain 25% variance and is non-negligible. Therefore, it is necessary to
 284 consider both the barotropic and first baroclinic modes in reconstructing of the full velocity.

285 The connection between the two vertical normal modes can also be understood from the
 286 time variability. First, the correlation of the time series between the barotropic mode and the first
 287 baroclinic mode is 0.77. Moreover, the ratio between the time series amplitude of the barotropic
 288 mode ($P_0(t)$) and the first baroclinic mode ($P_1(t)$) is 0.21, while the strength ratio between these
 289 two modes in the deepest layer ($r_c = |C_1(H)|/|C_0(H)|$) is 0.196. Therefore, it is reasonable to
 290 infer that the barotropic mode and first baroclinic mode neutralize each other at the bottom.
 291 Since the barotropic mode is depth independent, we could linearly add it up with the first
 292 baroclinic mode by taking a weight of r_c ,

$$293 \quad C_s(z) = C_1(z) + r_c C_0(z). \quad (3)$$

294 As a result, we obtain a summed mode ($C_s(z)$) combining the first two vertical normal modes,
 295 which is similar to the EOF1. To better understand the relationship between the dominant EOF1
 296 and the summed vertical modes ($C_s(z)$), we have normalized these two modes ($C_s(z)$ and EOF1)
 297 to 1 at the surface before further analysis. Figure 3a shows the profile of these two modes, whose
 298 vertical structures are nearly identical. It should be noted that the EOF1 only uses the observed
 299 velocity, while the summed vertical normal mode, on the contrary, only uses the hydrostatic data.
 300 Despite different methods, the consistency between the two modes (Figure 3a, b) indicates both
 301 the EOF decomposition and the vertical mode decomposition can well capture the main vertical
 302 structure.

303 To investigate the strength of the observed velocity projected onto the main mode of the
 304 two methods, we further calculate the projection coefficients using Equation (2a). The projection
 305 coefficients of the two modes are nearly identical, which further demonstrates their consistency
 306 (Figure 3b). Therefore, the PC1 could be well reproduced by linearly combining the barotropic and
 307 first baroclinic vertical normal modes ($P_s(t)$). Both these two main vertical modes are
 308 normalized to 1 at the surface, therefore, the projection coefficients (PC1 and $P_s(t)$) represent the
 309 strength of the surface flow. For the oceanic currents, if we focus on low-frequency and large-
 310 scale movement, these currents can be treated as geostrophic flows. The surface geostrophic flow
 311 could be easily derived from AVISO altimetry data. Figure 3b shows the time series of AVISO
 312 geostrophic flow anomaly (u'_g), the PC1, and the $P_s(t)$. Since the EOF decomposition has
 313 removed the statistical mean, we also calculated the anomaly of the geostrophic flow to focus on
 314 the time variability. The correlations between u'_g and the time series of the two modes are 0.86
 315 ($P_s(t)$) and 0.87 (PC1). These consistencies show that the surface geostrophic flow anomaly
 316 could be well treated as an approximation of the projection coefficients.

317 3.4 Other Mooring Sites

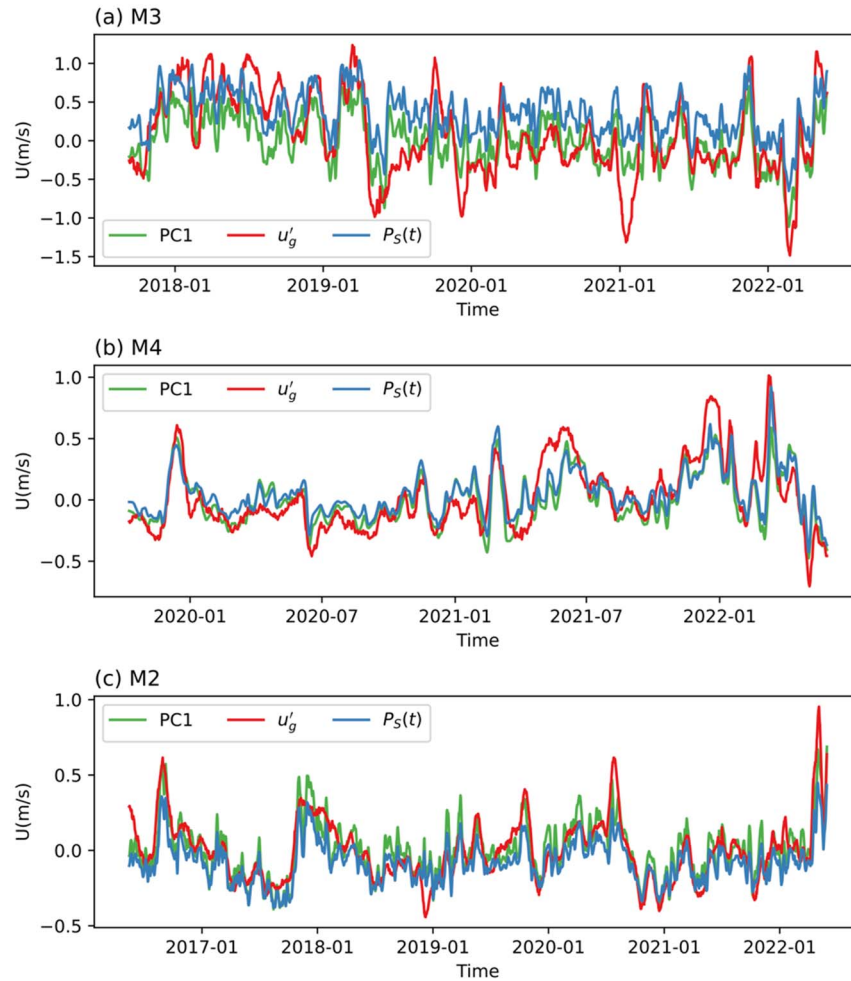
318 To estimate the KE transport, it is necessary to extend this relationship to other mooring
 319 sites. Following the analysis at the M1, we also conducted two types of mode decomposition for
 320 other moorings. The zero crossing of the first baroclinic mode deepens at high latitude, with
 321 values of 1500 m (M1), 1630 m (M3), 1750 m (M4), and 1800 m (M2). This is easy to

322 understand since the temperature in the upper layer drops as latitude increases, which results in a
 323 weak stratification and a large vertical scale of the upper layer ocean. Consequently, the flow at a
 324 high latitude becomes more barotropic and the ratio between the strength of barotropic and first
 325 baroclinic modes (r_c) also increases as the latitude increases (Table 1). Although the vertical
 326 structures slightly vary at different sites, the observed horizontal velocity could also be well
 327 reproduced by the first two modes, which explains over 80% variance for other sites (Table 1).
 328 The explained variance of EOF1 is slightly larger than the vertical normal modes. That's not
 329 surprising because the EOF1 may contain higher baroclinic modes, which results in a tiny
 330 difference (Figure 3a). However, the explained variance of these higher baroclinic modes is
 331 relatively small, so we can neglect them.

332 Table 1 The ratio between the strength of the barotropic and first baroclinic modes, the explained
 333 variance of the summed vertical mode and EOF1 mode, and the correlations between the AVISO
 334 geostrophic velocity and these two modes (PC1 and $P_s(t)$) for all sites.

	M1 (32.4°N)	M3(35°N)	M4(37°N)	M2(39°N)
r_c	0.196	0.200	0.231	0.259
Var ($C_s(z)$)	82%	82%	88%	85%
Var (PC1)	92%	90%	89%	88%
Cor ($u'_g, P_s(t)$)	0.86	0.83	0.72	0.83
Cor ($u'_g, PC1$)	0.87	0.84	0.73	0.83

335



336

337

Figure 4 Same as Figure 3b but for the M3 (a), M4 (b), and M2 (c) sites.

338

339

340

341

342

343

344

345

346

347

348

349

3.5 Vertical Structure of KE in OFES

350

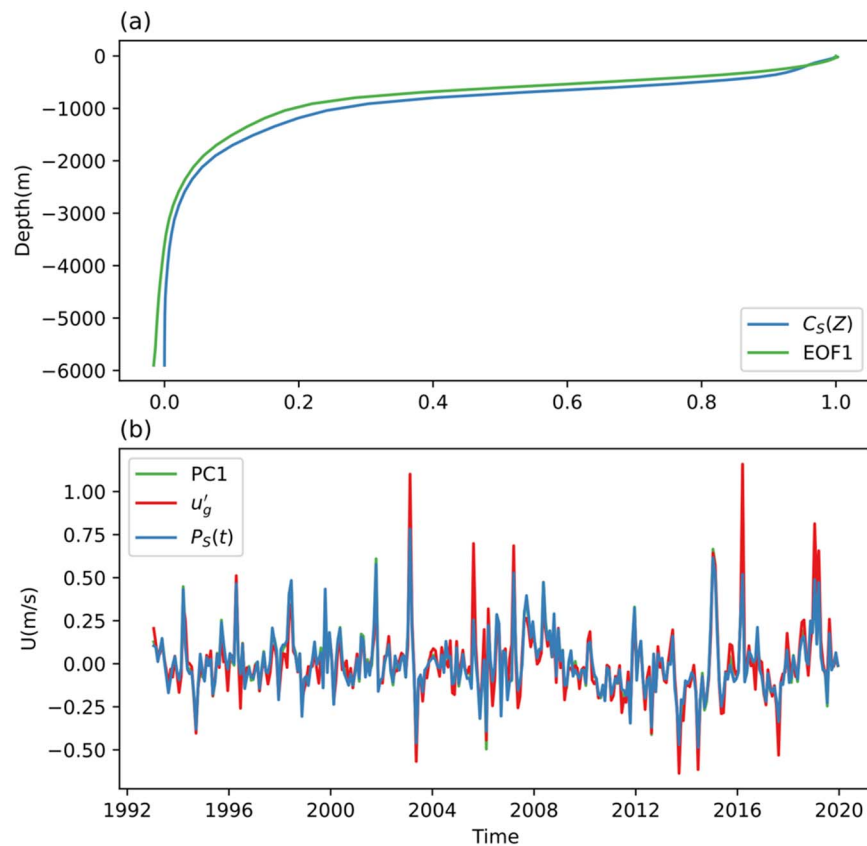
351

352

353

Combining two mode decomposition methods suggests a dynamic relationship between the vertical structure of the zonal velocity and the altimetry observed geostrophic current, but four moorings are too sparse to sufficiently cover the KE jet. To examine if this relationship can hold in the entire KE region, we extend this method to the OFES dataset. We first applied this method

354 at the same position as the M1 site in the OFES. Figure 4 shows the EOF1, the summed vertical
 355 mode, and the projection coefficients of these two modes. Both the vertical structure and the
 356 variability exhibit high similarity between EOF and summed vertical mode. Since we could use
 357 the time-dependent hydrographic data in OFES to calculate the stratification, we could eliminate
 358 the effect of eddies coming from other regions. Not surprisingly, the performance of mode
 359 decomposition in the OFES simulation is much better than the observed results based on the
 360 WOA18 data. It is interesting to note that there still exist some strong peaks, where the
 361 geostrophic current and the projection coefficient show an obvious difference. This is not
 362 surprising, since for strong eddy the nonlinearity and centrifugal force (Zhu et al., 2020) cannot
 363 be ignored, which will break the geostrophic balance. The results at other sites are essentially the
 364 same as the M1 (not shown), which implies that this dynamic relationship also holds at other
 365 sites in the OFES data.



366

367

Figure 5 Same as Figure 3 but for the OFES dataset.

368

369

370

371

372

373

374

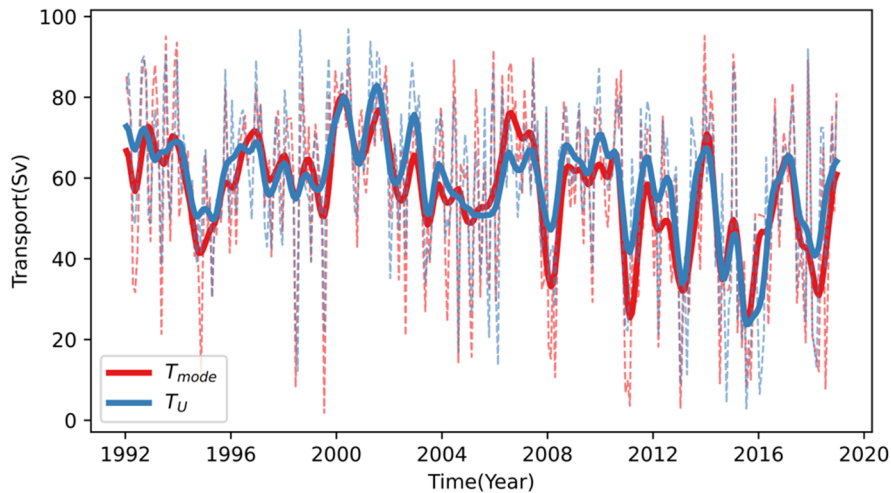
375

376

377

To further test the ability of the mode decomposition methods to reproduce the KE transport, it is necessary to extend this method to the entire KE region. The OFES could provide full-depth velocity as well as the surface geostrophic flow, which is helpful to directly calculate the transport and estimate the transport base on mode decomposition. Since the line between the M1 and M4 sites could well cover the KE jet (Figure 1), we first reproduced the vertical profile of the horizontal velocity by using the hydrostatic data and the modeled sea surface height along the mooring track from M1 to M4. It should be noted that the summed vertical modes and the EOF mode represent the variability without the statistical mean (Figure 4). Therefore, the climatologic velocities were added to the reconstructed velocities. Then we calculated the cross-sectional transport based on the reconstructed velocity and the velocity directly derived from the

378 model, respectively. Figure 6 shows these two types of transport from 1993 to 2019. The
 379 consistency between these two types of transport shows that the mode reconstruction method
 380 could reproduce cross-sectional transport well, including its strength and variability (Figure 6).
 381 The averaged transport directly calculated from the modeled velocities is $58.3+11.9$ Sv, while the
 382 averaged reconstructed transport is $54.7+14.4$ Sv. As for the variability, the correlation between
 383 the modeled transport and the reconstructed transport is 0.88. We can confidently conclude that
 384 the dominant features of the barotropic and first baroclinic modes hold in the entire KE region,
 385 which can support the estimation of the KE transport.



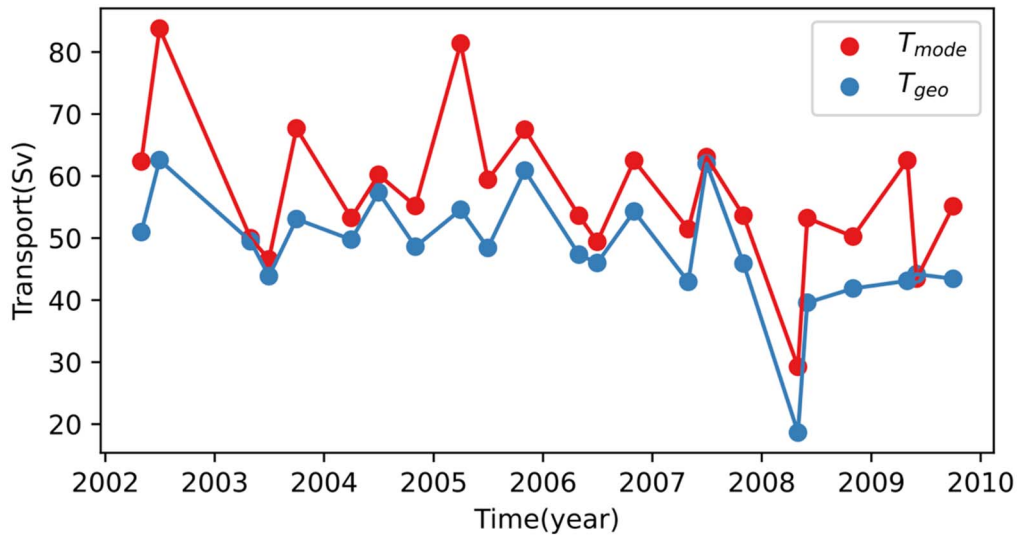
386
 387 Figure 6 The cross-sectional transport from M1 to M2 using the OFES modeled velocity (blue)
 388 and reconstructed velocity (red), respectively. The dashed lines denote the monthly mean
 389 transport and the solid lines denote the low-pass filtered transport with a 13 months cutoff.

390 3.6 Estimated KE Transport

391 Next, we apply this method in the real ocean to estimate the KE transport by combining the
 392 AVISO geostrophic velocity and the WOA T/S data. Since the mode estimation method was
 393 based on the geostrophic balance and may be affected by high-frequency variability when there
 394 were strong currents, we use the monthly mean geostrophic flow from the AVISO datasets. The
 395 monthly climatological WOA T/S data are used to compute the vertical normal mode and
 396 background geostrophic velocity.

397 Before further comparison, it is noteworthy that the relationship between vertical normal
 398 mode and EOF mode will lose its adaptability near the coastal region, where the Kuroshio
 399 current could extend to the bottom. In this case, the bottom current is not weaker than the upper
 400 layer flow, which will make it impossible to linearly sum up the barotropic and first baroclinic
 401 modes. Therefore, we chose some historical sections away from the Japanese coast for
 402 comparison. We first provide a comparison of the KE transport along the 147°E line with
 403 observation based on absolute geostrophic velocity (Long et al., 2019). Absolute geostrophic
 404 velocity along the 147°E line was obtained from hydrographic data. The averaged cross-section
 405 transport from 30°N to 40°N at this section is 48.2 ± 9.0 Sv based on the inverse method, while
 406 the mode reconstructed transport ($57.2+11.3$ Sv) is slightly stronger than observation. Despite
 407 this difference, the time variability of the KE transport is quite similar to the mode estimation. As
 408 shown in Figure 7, the observation is highly correlated with the mode estimation with a
 409 correlation reaching 0.81.

410



411 Figure 7 The volume transport across the 147°E line based on the hydrographic data (blue) and the
 412 mode reconstruction (red).
 413

414 Besides, Jayne et al. (2009) used combined observations from the KESS to estimate the
 415 strength and structure of the KE and its recirculation. Based on the Eulerian average, they gave
 416 an estimate of 79 Sv for the KE transport. The mode estimation method suggests an average
 417 transport of 85 Sv for the KE over the same period and the same location as the KESS, which is
 418 quite similar to its estimation. Based on Lowered ADCP data, Yoshikawa et al. (2004) showed
 419 that the eastward Kuroshio Extension transport was 163 Sv across 146°25'E in May 2001 and
 420 113 Sv across 152°30'E in July 2000. However, the mode estimation method gives 97 and 94 Sv
 421 in these two sections, which is weaker than the Lowered ADCP estimation. This reduction may
 422 be due to the smoothing effect using the monthly mean altimeter data, while the ADCP
 423 observation may contain non-geostrophic components.
 424

425 4 Summary and Discussion

426 In this study, we have investigated the vertical structure of the zonal velocity in the
 427 Kuroshio Extension region using a mooring array. The vertical structure of the zonal velocity is
 428 dominated by the barotropic and first baroclinic modes, which explain over 80% variance for all
 429 mooring sites. This structure is also well reproduced by EOF decomposition, where the EOF1
 430 contains mixed signals from these two modes. By connecting the vertical normal modes and
 431 EOF1 mode, a new transport estimation method is proposed to estimate the Kuroshio Extension
 432 transport.

433 The first baroclinic mode contributes most to the full velocity in all sites, which is surface
 434 intensified and reverses in the deep layer with a zero-crossing depth range from 1500 m to 1800
 435 m as latitude increases. However, using this single mode will largely underestimate the full
 436 velocity. The barotropic mode is depth independent, strengthening the upper layer flow and
 437 weakening the deep layer flow. Moreover, the EOF1 also drops from the surface to the deep
 438 ocean but does not reverse, which contains a mixed signal of barotropic and first baroclinic
 439 modes. Therefore, it is reasonable to assume that the barotropic and first baroclinic modes tend
 440 to cancel each other at the bottom, and we could linearly sum up these two modes. The

441 projection coefficients of the summed vertical mode and the PC1 are nearly identical. Since the
442 vertical profiles of the dominant vertical mode from the two methods (EOF1 and $C_s(z)$) are
443 normalized to 1 at the surface, the projection coefficients (PC1 and $P_s(t)$) could be approximated
444 by the surface geostrophic current flow.

445 Therefore, we found a remarkable relationship that connects the surface geostrophic current
446 and the vertical structure of the zonal current in the KE region. This relationship is tested
447 extensively for the whole KE region by using the OFES datasets, which shows that this
448 relationship could hold in the whole KE region. Then we use this method to estimate the KE
449 transport and compare it with some historical sections. The estimated KE transport is generally
450 in agreement with the observations along the 147°E line and the KESS observation (Jayne et al.,
451 2009). These results show that the mode estimation method could well reproduce the KE
452 transport. This method provides a more direct estimation of the KE and its vertical structure,
453 which can be calculated using AVISO geostrophic flow and WOA hydrographic data.
454 Furthermore, the KE transport is easy to be estimated based on the vertical structure, which is an
455 essential basis for studying the climate influences of the KE.

456 It should be noted that the projection coefficient is weaker than the surface geostrophic
457 current for some strong currents. A detailed check shows that the vertical structure will be
458 affected by non-local eddies. These eddies will bring seawater with different hydrographic
459 information, which contaminates the local vertical structure. This feature will be improved by
460 using time-dependent T/S data in OFES. However, even in the OFES, there are still some peaks
461 where the geostrophic current is stronger than the mode projection coefficient. This is because
462 we have not taken centrifugal force or non-linear terms into consideration, which will break the
463 geostrophic balance, especially for strong eddies. Nevertheless, this mode estimation method
464 could well reproduce the main structure and over 80% variance of the KE transport.
465

466 **Acknowledgments**

467 This research is financially supported by the National Natural Science Foundation of China
468 (42225601, 42076009, 42176006), and Fundamental Research Funds for the Central Universities
469 (202072001, 202241006). Z. Chen is partly supported by the Taishan Scholar Funds
470 (tsqn201812022).
471

472 **Data Availability Statement**

473 The mooring data are available at the Kuroshio Extension Mooring System website (<https://cn-kems.net/Data/data.zip.001>; <https://cn-kems.net/Data/data.zip.002>). The AVISO data are
474 available at <https://sso.altimetry.fr/>. The World WOA 18 data are available at
475 <https://www.ncei.noaa.gov/archive/accession/NCEI-WOA18>. The OFES data are downloaded
476 from University of Hawaii website <https://apdrc.soest.hawaii.edu/datadoc/ofes/ofes.php>.
477 Hydrographic data from and 147°E section is downloaded from Japan Meteorological Agency
478 website http://www.data.jma.go.jp/gmd/kaiyou/db/vessel_obs/data-report/html/ship/ship.php.
479
480

481 **References**

- 482 Bishop, S. P., Watts, D. R., Park, J. H., & Hogg G., N. G. (2012). Evidence of bottom-trapped
483 currents in the Kuroshio Extension region. *Journal of Physical Oceanography*, *42*(2), 321–328.
484 doi:10.1175/JPO-D-11-0144.1
- 485 Ducet, N., Le Traon, P. Y., & Reverdin, G. (2000). Global high-resolution mapping of ocean
486 circulation from TOPEX/Poseidon and ERS-1 and -2. *Journal of Geophysical Research: Oceans*,
487 *105*(C8), 19477–19498. doi:10.1029/2000jc900063
- 488 Hall, M. M. (1989). Velocity and transport structure of the Kuroshio Extension at 35°N, 152°E.
489 *Journal of Geophysical Research*, *94*(C10), 14445. doi:10.1029/JC094iC10p14445
- 490 Hiroe, Y., Yasuda, I., Komatsu, K., Kawasaki, K., Joyce, T. M., & Bahr, F. (2002). Transport of
491 North Pacific intermediate water in the Kuroshio-Oyashio interfrontal zone. *Deep-Sea Research*
492 *Part II: Topical Studies in Oceanography*, *49*(24–25), 5353–5364. doi:10.1016/S0967-
493 0645(02)00195-9
- 494 Hurlburt, H. E., Wallcraft, A. J., Schmitz, W. J., Hogan, P. J., & Metzger, E. J. (1996). Dynamics
495 of the Kuroshio/Oyashio current system using eddy-resolving models of the North Pacific
496 Ocean. *Journal of Geophysical Research: Oceans*, *101*(C1), 941–976. doi:10.1029/95JC01674
- 497 Jayne, S. R., Hogg, N. G., Waterman, S. N., Rainville, L., Donohue, K. A., Randolph Watts, D.,
498 et al. (2009). The Kuroshio Extension and its recirculation gyres. *Deep Sea Research Part I:*
499 *Oceanographic Research Papers*, *56*(12), 2088–2099. doi:10.1016/j.dsr.2009.08.006
- 500 Joyce, T. M. (1987). Hydrographic sections across the Kuroshio extension at 165°E and 175°W.
501 *Deep Sea Research Part A, Oceanographic Research Papers*, *34*(8), 1331–1352.
502 doi:10.1016/0198-0149(87)90130-0

- 503 Kalnay, E., Kanamitsu, M., Kistler, R., Collins, W., Deaven, D., Gandin, L., et al. (1996). The
504 NCEP/NCAR 40-Year Reanalysis Project. *Bulletin of the American Meteorological Society*,
505 77(3), 437–471. doi:10.1175/1520-0477(1996)077<0437:TNYRP>2.0.CO;2
- 506 Kida, S., Mitsudera, H., Aoki, S., Guo, X., Ito, S. ichi, Kobashi, F., et al. (2015). Oceanic fronts
507 and jets around Japan: a review. *Journal of Oceanography*, 71(5), 469–497. doi:10.1007/s10872-
508 015-0283-7
- 509 Locarnini, R. A., Mishonov, A. V., Baranova, O. K., Boyer, T. P., Zweng, M. M., Garcia, H. E.,
510 et al. (2019). World Ocean Atlas 2018, Volume 1: Temperature. A. Mishonov, Technical Editor.
511 *NOAA Atlas NESDIS*, 81(July), 52.
- 512 Long, Y., Zhu, X. H., & Guo, X. (2019). The Oyashio Nutrient Stream and Its Nutrient Transport
513 to the Mixed Water Region. *Geophysical Research Letters*, 46(3), 1513–1520.
514 doi:10.1029/2018GL081497
- 515 Long, Y., Zhu, X. H., Guo, X., & Huang, H. (2018). Temporal Variation of Kuroshio Nutrient
516 Stream South of Japan. *Journal of Geophysical Research: Oceans*, 123(11), 7896–7913.
517 doi:10.1029/2017JC013635
- 518 Ma, X., Jing, Z., Chang, P., Liu, X., Montuoro, R., Small, R. J., et al. (2016). Western boundary
519 currents regulated by interaction between ocean eddies and the atmosphere. *Nature*, 535(7613),
520 533–537. doi:10.1038/nature18640
- 521 Ma, J., Hu, S., Hu, D., Villanoy, C., Wang, Q., Lu, X., & Yuan, X. (2022). Structure and
522 Variability of the Kuroshio and Luzon Undercurrent Observed by a Mooring Array. *Journal of*
523 *Geophysical Research: Oceans*, 127(2), 1–12. doi:10.1029/2021jc017754

- 524 Masumoto, Y., Sasaki, H., Kagimoto, T., Komori, N., Ishida, A., Sasai, Y., et al. (2004). A Fifty-
525 Year Eddy-Resolving Simulation of the World Ocean - Preliminary Outcomes of OFES (OGCM
526 for the Earth Simulator). *Journal of the Earth Simulator*, *1*, 35–56.
- 527 Oliver, E. C. J., Benthuisen, J. A., Darmaraki, S., Donat, M. G., Hobday, A. J., Holbrook, N. J.,
528 et al. (2021). Marine Heatwaves. *Annual Review of Marine Science*, *13*, 313–342.
529 doi:10.1146/annurev-marine-032720-095144
- 530 Qiu, B. (2003). Kuroshio extension variability and forcing of the Pacific decadal oscillations:
531 Responses and potential feedback. *Journal of Physical Oceanography*, *33*(12), 2465–2482.
532 doi:10.1175/2459.1
- 533 Qiu, B., Chen, S., & Hacker, P. (2007). Effect of mesoscale eddies on subtropical mode water
534 variability from the Kuroshio Extension System Study (KESS). *Journal of Physical*
535 *Oceanography*, *37*(4), 982–1000. doi:10.1175/JPO3097.1
- 536 Ren, Q., Li, Y., Wang, F., Song, L., Liu, C., & Zhai, F. (2018). Seasonality of the Mindanao
537 Current/Undercurrent System. *Journal of Geophysical Research: Oceans*, *123*(2), 1105–1122.
538 doi:10.1002/2017JC013474
- 539 Suga, T., & Hanawa, K. (1995). The Subtropical Mode Water Circulation in the North Pacific.
540 *Journal of Physical Oceanography*, *25*(5), 958–970. doi:10.1175/1520-
541 0485(1995)025<0958:TSMWCI>2.0.CO;2
- 542 Talley, L. D., Nagata, Y., Fujimura, M., Iwao, T., Kono, T., Inagake, D., et al. (1995). North
543 Pacific Intermediate Water in the Kuroshio/Oyashio Mixed Water Region. *Journal of Physical*
544 *Oceanography*, *25*(4), 475–501. doi:10.1175/1520-0485(1995)025<0475:NPIWIT>2.0.CO;2

- 545 Tsunogai, S., Ono, T., & Watanabe, S. (1993). Increase in total carbonate in the western North
546 Pacific water and a hypothesis on the missing sink of anthropogenic carbon. *Journal of*
547 *Oceanography*, *49*(3), 305–315. doi:10.1007/BF02269568
- 548 Vallis, G. K. (2017). *Atmospheric and oceanic fluid dynamics*. Cambridge University Press.
- 549 Yang, Y., Liang, X. S., & Sasaki, H. (2021). Vertical coupling and dynamical source for the
550 intraseasonal variability in the deep Kuroshio Extension. *Ocean Dynamics*, *71*(11–12), 1069–
551 1086. doi:10.1007/s10236-021-01482-9
- 552 Yasuda, I. (2004). North Pacific intermediate water: Progress in SAGE (SubArctic Gyre
553 Experiment) and related projects. *Journal of Oceanography*, *60*(2), 385–395.
554 doi:10.1023/B:JOCE.0000038344.25081.42
- 555 Yoshikawa, Y., Church, J. A., Uchida, H., & White, N. J. (2004). Near bottom currents and their
556 relation to the transport in the Kuroshio Extension. *Geophysical Research Letters*, *31*(16), 1–5.
557 doi:10.1029/2004GL020068
- 558 Zhu, R., Chen, Z., Zhang, Z., Yang, H., & Wu, L. (2020). Subthermocline Eddies in the
559 Kuroshio Extension Region Observed by Mooring Arrays. *Journal of Physical Oceanography*,
560 *51*(2), 439–455. doi:10.1175/jpo-d-20-0047.1
- 561 Zweng, M. M., Reagan, J. R., Seidov, D., Boyer, T. P., Antonov, J. I., Locarnini, R. A., et al.
562 (2019). World Ocean Atlas 2018 Volume 2: Salinity. *NOAA Atlas NESDIS*, *82*(July), 50pp.
563 Retrieved from http://www.ncei.noaa.gov/sites/default/files/2020-04/woa18_vol2.pdf